Strong-interaction effect measurements in sigma hyperonic atoms of W and Pb

R. J. Powers, M. Eckhause, P. P. Guss,* A. D. Hancock, D. W. Hertzog, †
D. Joyce,‡ J. R. Kane, W. C. Phillips,§ W. F. Vulcan,‡ R. E. Welsh,
R. J. Whyley,** and R. G. Winter

College of William and Mary, Williamsburg, Virginia 23187

E. Austin, G. W. Dodson,†† J. P. Miller, F. O'Brien,‡‡ B. L. Roberts,
and D. R. Tieger††

Boston University, Boston, Massachusetts 02215

R. B. Sutton

Carnegie-Mellon University, Pittsburgh, Pennsylvania 15213

R. Kunselman

University of Wyoming, Laramie, Wyoming 82071

(Received 7 October 1992)

Strong-interaction effects have been observed in the x-ray spectra of atoms formed with Σ^- hyperons in W and Pb. The spectra were analyzed for energy shifts and broadenings and for yield reductions of the final x-ray transitions before absorption of the Σ^- by the nucleus. The results for the $10l \rightarrow 9k$ transitions of Σ^- hyperonic atoms averaged over fine structure components are ^{184}W: $\varepsilon(9k) = 214 \pm 60$ eV, $\Gamma(9k) = 18 \pm 149$ eV, $\Gamma(10l) = 2 \pm 2$ eV; ^{208}Pb: $\varepsilon(9k) = 422 \pm 56$ eV, $\Gamma(9k) = 428 \pm 158$ eV, $\Gamma(10l) = 17 \pm 3$ eV, where the strong interaction shift $\varepsilon = E_m - E_c$, E_m is the measured transition energy, and E_c is the transition energy calculated assuming no strong interaction and Γ is the Lorentzian broadening. A four-parameter optical potential representing an effective spin-independent Σ^--nuclear hadronic interaction was fitted by these results in combination with previous data from lower-Z nuclei.

PACS number(s): 21.30.+y, 25.80.Pw, 36.10.Gv

I. INTRODUCTION

An exotic atom is formed when a negatively charged particle other than an electron is captured into an atomic orbit around a nucleus. The x rays emitted by such exotic atoms can provide information regarding the orbiting particle, the nucleus, and the interaction between the particle and the nucleus. We present here data regarding the strong interaction of Σ^- hyperons with heavy nuclei.

After capture into an initial atomic orbit, the Σ^- cascades through states of successively lower energies that bring it closer to the nucleus. At the beginning of the cascade when the Σ^- has substantial overlap with electron states, deexcitation occurs primarily through Auger transitions, whose energies are modified appreciably by electron screening. When the Σ^- reaches states that lie mostly inside the electron cloud, deexcitation occurs predominantly through x-ray emission. The energies of these x rays are determined primarily by the electromagnetic interaction between the nucleus and the Σ^-, and are useful for determining properties of the Σ^- hyperon. We have published the results of our determination of the magnetic dipole moment [1] and the mass of the Σ^- [2] from the x rays emitted in transitions between such states.

When the Σ^- reaches a state which has appreciable overlap with the nucleus, the intensities of the x-ray transitions are reduced by strong nuclear capture of the Σ^-, and the energy levels are shifted and broadened by the strong interaction. The data from this domain provide Σ^--nucleus strong interaction information, which is generally parametrized in terms of an "effective" complex scattering length.

Strong absorption increases abruptly as the Σ^- cascades, so that only a few states give strong-interaction information. Generally, only the last state reached by an electromagnetic transition of appreciable yield shows a

---

*Present address: EG&G Energy Measurements, Suitland, MD 20746.

†Present address: Department of Physics, University of Illinois, Urbana, IL 61801.

‡Present address: CEBAF, Newport News, VA 23606.

§Present address: Bell Communications Research, Red Bank, NJ 07701.

**Present address: MCI Telecommunications Inc., Colorado Springs, CO 80902.

††Present address: Massachusetts Institute of Technology, Laboratory for Nuclear Science, Cambridge, MA 02139.

‡‡Present address: AT&T Bell Laboratories, Whippany, NJ 07981.

measurable shift and broadening. The measurement of the intensities of transitions to this last state provides a means of determining the nuclear capture rate from the initial states and hence the broadenings of the upper states.

The present paper describes the measurement of the energies and intensities of x rays from the $10l \rightarrow 9k$ transitions of Σ^- in W and Pb, and the determination of an "effective" complex Σ^--nucleus scattering length from these measurements.

Various considerations are involved in the proper interpretation of the x-ray data [1–3]. The theoretical atomic calculations needed in order to extract the strong interaction effects will be discussed in the next section. In Sec. III we briefly describe the experimental details. Section IV contains a discussion of the data analysis. The results are given in Sec. V and Sec. VI comprises a discussion of our results.

II. THEORETICAL DETAILS

A. Solution to the Dirac equation

In the absence of strong interactions the determination of the bound energy levels of a fermion such as a Σ^- hyperon in the presence of a nuclear Coulomb field is straightforward and in principle can be calculated with arbitrarily small uncertainty. The techniques have been discussed by Borie [4] and by Borie and Jödicke [5] for antiprotonic atoms.

The Dirac equation for Σ^- hyperonic atoms was solved numerically using the program developed for muonic atoms, which is discussed elsewhere [6]. Eigenvalues were obtained for a potential that included the Coulomb interaction and effects due to vacuum polarization [7] in first order with the average experimental value of the Σ^- hy-

peron mass given by the Particle Data Group [8]. Higher-order vacuum polarization corrections of Blomqvist [9] up to seventh order were made by perturbation techniques as were all other corrections. An additional correction for the finite size vacuum polarization of orders higher than $\alpha(Z\alpha)$ as described by Borie and Jödicke [5] was included. Screening corrections have been taken from the work of Vogel [10]. Self-energy terms [11] were calculated and included a correction for the anomalous magnetic moment of the Σ^- as obtained from the fine-structure splitting measured by Hertzog *et al.* [1] with the same apparatus. Nuclear polarization corrections were made using the nuclear polarizability given by Ericson and Hüfner [12] following the technique of Borie and Jödicke [5]. The relativistic center-of-mass motion correction has been discussed by Fricke [13] and by Friar and Negele [14]. As Borie [4] points out, the only significant contribution for high-Z antiprotonic and Σ^- atoms is the leading term $B_0^2/2m_N$, where B_0 is the binding energy of the Σ^- and m_N is the mass of the nucleus. A summary of the binding energies of relevant Σ^- atomic levels in Pb and W is given in Table I. The nuclear charge parameters used in calculating the electromagnetic effects are listed in Table II.

In addition to the nuclear polarization correction mentioned above, we calculated explicitly the dynamic $E2$ excitations of low-lying levels in W. Since all of the isotopes have ground-state spin $I=0$ or $1/2$, there is no static $E2$ hyperfine structure (hfs). However, there is still an appreciable correction due to dynamic $E2$ excitation of the nuclei, since the energies of the first excited levels of all these strongly deformed isotopes ($Q_0 \approx 7$ b) are only about 100 keV. This effect has been discussed by Hitlin *et al.* [15] for the case of muonic $2p$ and $3d$ levels where the $E2$ mixing matrix elements are of comparable size to those in Σ^- $10l$ and $9k$ levels. We have used the

TABLE I. Electromagnetic contributions to Σ^- binding energies (keV).

Z	A	State	Dirac solution[a]	Electron screening	Higher order vac. pol.	Nuclear polarization	$E2$ dynamic shift	Total
82	208	$13n23/2$	1265.589	0.079	−0.079	0.010	0.0	1265.599
		$13n21/2$	1266.076	0.079	−0.079	0.010	0.0	1266.086
		$11m21/2$	1768.897	0.040	−0.109	0.024	0.0	1768.852
		$11m19/2$	1769.862	0.040	−0.109	0.024	0.0	1769.817
		$10l19/2$	2141.702	0.030	−0.126	0.051	0.0	2141.657
		$10l17/2$	2143.273	0.030	−0.126	0.051	0.0	2143.228
		$9k17/2$	2646.012	0.021	−0.145	0.122	0.0	2646.110
		$9k15/2$	2648.727	0.021	−0.145	0.123	0.0	2648.726
74	184	$13n23/2$	1029.498	0.055	−0.047	0.005	0.010	1029.521
		$13n21/2$	1029.819	0.055	−0.047	0.005	0.010	1029.842
		$11m21/2$	1438.884	0.028	−0.064	0.012	0.047	1438.913
		$11m19/2$	1439.523	0.028	−0.064	0.012	0.047	1439.546
		$10l19/2$	1742.078	0.020	−0.073	0.027	0.150	1742.202
		$10l17/2$	1743.118	0.020	−0.073	0.027	0.151	1743.243
		$9k17/2$	2152.210	0.014	−0.081	0.066	0.548	2152.757
		$9k15/2$	2153.997	0.014	−0.081	0.066	0.544	2154.540

[a]The Dirac solution includes finite size Coulomb correction, anomalous magnetic moment of the Σ^- hyperon, and first-order vacuum polarization for the mass and magnetic moment given in Ref. [8] and Ref. [1], respectively.

TABLE II.   Isotopic properties of W and Pb.

Z	A	Nuclear charge distribution parameters[a]				Isotopic abundance (%)	Energy[b] 2^+ level (keV)
		$c/A^{1/3}$ (fm)	t (fm)	β	Q_0 (e b)		
74	182	1.131	2.118	0.248	6.58	26.3	100.1
	183	1.1295	2.1425	0.2425	6.43	14.3	78.0
	184	1.128	2.167	0.237	6.29	30.7	111.2
	186	1.132	2.100	0.222	5.92	28.6	122.5
82	206	1.1243	2.306	0.0	0.0	24.1	—
	207	1.1221	2.333	0.0	0.0	22.1	—
	208	1.1208	2.344	0.0	0.0	52.3	—

[a]The nuclear charge parameters for tungsten were taken from Ref. [15] except for [183]W, whose values were interpolated from the adjacent even isotopes. The charge parameters for Pb were taken from Ref. [16]. A 3-parameter deformed Fermi distribution was used for the nuclear charge density.

[b]The energies of the first 2^+ level, which were used in the calculation of the dynamic $E2$ shift, were taken from Ref. [32]. For the spin-$\frac{1}{2}$ odd nucleus [183]W, we took a spin-weighted average of the first $3/2^-$ and $5/2^-$ levels.

intrinsic quadrupole moments Q_0 measured by Hitlin *et al.* and given in Table II to calculate the shifts of the Σ^- energy levels, which are given in Table I. The radial matrix elements described by Hitlin *et al.* were calculated for the wave functions associated with the solution of the Dirac equation as described above.

The uncertainty of these electromagnetic calculations is dominated by the uncertainties in the measured mass of the Σ^- hyperon as well as the uncertainties of the nuclear polarization corrections (20%) and the dynamic $E2$ shifts (5%). These errors amount to about one third of the experimental uncertainties.

B. Strong interactions

Once the electromagnetic effects have been calculated, it is straightforward to add an effective optical potential to the electromagnetic potential in the solution of the Dirac equation to represent the hadronic interaction between the Σ^- and the nucleus. The form of the optical potential presently used to describe strong interaction effects in Σ^- atoms has been discussed by Batty [17, 18]. Since experimental data are not very precise, the following spin-independent form is believed to be adequate:

$$V = -\frac{2\pi}{\mu}(1+\mu/M)[a_0(\rho_n(r)+\rho_p(r))+a_1(\rho_n(r)-\rho_p(r))].$$

(1)

Here, μ is the Σ^--nucleus reduced mass, M is the nucleon mass, $\rho_n(r)$ and $\rho_p(r)$ are the radial neutron and proton nuclear densities normalized to the appropriate number of neutrons and protons respectively, and a_0 and a_1 are the complex isoscalar and isovector scattering lengths for the Σ^--nucleon hadronic interaction. In the past [18] isospin independence was assumed, i.e. a_1 has been taken to be zero. In this work we shall examine how well existing Σ-atomic strong interaction data determine the two complex terms in the optical potential. A discussion of alternative forms for the optical potential is given in the work of Yamada *et al.* [19].

The proton densities were obtained by unfolding the

nucleon form factors [20] from the charge densities, whose parameters are listed in Table II. The procedure is discussed in more detail in the work of Kunselman *et al.* [21]. The neutron densities were obtained from the theoretical values for Δ_{n-p}, the difference in the mean square radii of the neutron and proton densities, calculated with Hartree-Fock methods [22, 23].

As a matter of convenience (since we are ignoring the spin-dependence of the Σ^--nucleon hadronic interaction), we have used the Klein-Gordon program discussed elsewhere [24] to determine the strong interaction shifts and widths of the Σ^- levels.

III. EXPERIMENTAL DETAILS

The data were collected during the course of Experiment 723 performed at the Alternating Gradient Synchrotron (AGS) facility of Brookhaven National Laboratory (BNL). In addition a background run with pions was made at the Los Alamos Meson Physics Facility (LAMPF) to study the yield of possible contaminating γ rays caused by pions. The main purpose of the experiment was to determine the magnetic moment of the Σ^- hyperon from measurements of the fine structure of the x rays emitted by high-Z Σ^- atoms. The experiment was thus designed to produce and identify Σ^- atoms and measure the energies of the resulting deexcitation x rays [1, 2]. We have described the apparatus and its performance previously [1], and only review the essential points here.

In order for the short-lived Σ^- hyperons to survive decay, they must be produced with low kinetic energy by K^- particles interacting near the target atoms. Since the fine-structure splitting (which gives the Σ^- magnetic moment) is greater for transitions involving lower principal quantum numbers n, the energy region over which x rays were measured included the final few transitions before the orbiting Σ^- was absorbed by the nucleus. These final transitions are those in which strong interaction effects are most apparent. Thus, the basic requirements of the magnetic moment experiment provided at the same

time an excellent opportunity to study Σ^--nucleus strong interactions.

A. Beam line

The slow extracted mode of the BNL AGS was used. The beam period was approximately 2.8 s with a beam current of $\approx 10^{12}$ protons at a momentum of 28 GeV/c. The beam spill length ranged from 0.6 to 1.0 s.

Protons interacting in the C4 target (5 cm of Cu or Pt) produced kaons for this experiment. The C4 target beam line was tuned to select negatively charged kaons with momenta of 680 MeV/c. The beam had a momentum resolution of $\pm$ 2%. The predominant contaminants of the beam were pions, which outnumbered the kaons by a factor of about ten. For 4×10^{12} protons striking the production target during a single 800 ms beam spill, approximately 6×10^4 kaons were delivered to a point approximately 1 m downstream from the end of the C4 beam line.

B. Target, counters, and geometry

In previous Σ^- atom experiments [25, 26] the Σ^- were produced by reactions on nuclei in the target material. For high-Z atoms, calculations [27] predict that such reactions have only a 5% branching ratio. This experiment employed a novel approach that was made possible because the comparable reaction in liquid hydrogen,

$$K^- p \text{ (at rest)} \rightarrow \Sigma^- \pi^+$$

has a branching ratio of 47% [28]. Thin sheets of the high-Z target material (Pb or W) were suspended vertically in a liquid hydrogen bath and turned edgewise to the beam. The beam line was tuned to maximize K^- stops in the liquid hydrogen, thus maximizing Σ^- production.

Since the initial state for Σ^- production in hydrogen is a two-body state at rest, the Σ^- and π^+ so produced were monoenergetic with equal but opposite momenta of 173 MeV/c. The Σ^- hyperons were produced with a kinetic energy of 12.4 MeV and had a range in liquid hydrogen (assuming no decay) of 0.95 cm. Many of these Σ^- hyperons which were produced in the liquid hydrogen traveled to and stopped in a sheet of target material. The π^+ mesons were produced with a kinetic energy of 82.6 MeV and usually exited the target volume.

Monte Carlo simulations during the planning stages of the experiment demonstrated that maximizing the signal-to-noise ratio of the Σ^- atom x-ray intensities was of paramount importance to the determination of the Σ^- magnetic moment. Since Σ^- atoms can be formed only after the interaction of a K^- in the target, care was taken to design an arrangement that could differentiate between stopping kaons and the more numerous beam pions, which generally were far too energetic to be brought to rest within the target volume. However, these beam pions produced many beam-coincident γ and x rays which could contribute to the background in the energy region of the Σ^- atom x rays.

A plan view of the experimental apparatus is shown in Fig. 1. For purposes of discussion the arrangement is divided into four functional groups: laminar target, KSTOP identification, pion spectrometers, and x-ray spectrometers.

Particles leaving the last quadrupole of the beam line were detected by coincident signals from counters S1 and S2. Next, a velocity-selective Čerenkov counter C differentiated between the Čerenkov light of the pions and kaons by detecting the difference in the angle of emission of the light. Light from a traversing kaon was totally internally reflected to a bank of six photomultiplier tubes. Light from the faster pions had a larger angle of emission, which exceeded the critical angle for reflection. At a beam momentum of 680 MeV/c, best performance of this counter was obtained when a coincidence among any four or more of the six phototubes was required. In this mode of operation, tests indicated a kaon detection efficiency of 94% and a pion rejection ratio of greater than 50:1.

Following the Čerenkov counter C, counter S3 detected particles entering the moderator. The moderator was a 14 cm thickness of Cu covering a 10 cm $\times$ 10 cm area. This moderator was surrounded on the left, right, top, and bottom by a tunnel veto scintillator V_1 designed to detect any beam particles or their reaction products which exited the moderator in a direction divergent from the beam path. Monte Carlo simulations predicted that about $50 \pm 2\%$ of the K^- entering the moderator would decay or interact within its volume.

Downstream of the moderator, hodoscope H shown in Fig. 1 was used to measure the position and size of the beam spot. This hodoscope consisted of three vertical and four horizontal strips of 0.32-cm-thick plastic scintillator overlapped to provide a spatial resolution of 5 bins horizontally and 7 bins vertically over the 10 cm $\times$ 10 cm area of the moderator's downstream face. A bit register
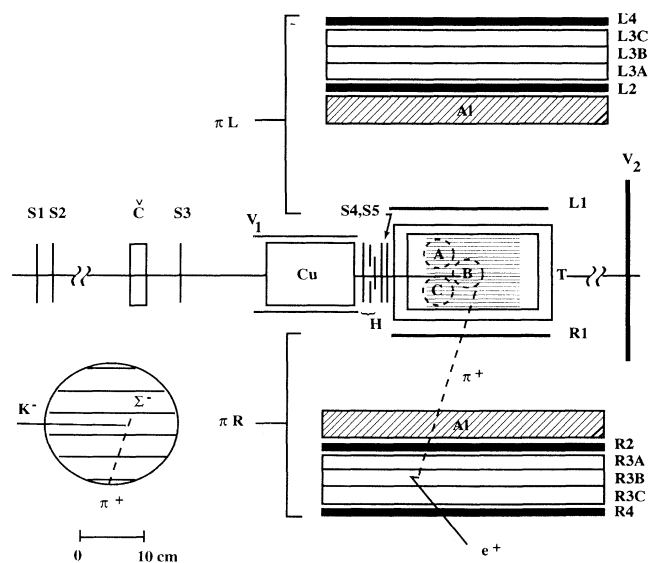
FIG. 1. A plan view of the experimental apparatus, including beam-defining plastic scintillators, π^+ spectrometers, and x-ray detectors (A, B, C) located below target (T).

was used to record the firing pattern of these counters, and this pattern was recorded as part of the event information.

The KSTOP identification system identified those beam particles with characteristics of a K^- stopping within the target volume. It also marked the time when beam particles entered the front face of the laminar target. The pion spectrometer was designed to detect and identify the π^+ associated with Σ^- production within the target volume. The x-ray spectroscopy system measured the energies of x rays emerging from the bottom of the laminar target. It also provided a time-mark signal for the x-ray event.

As shown in Fig. 1, a set of scintillation counters and aluminum moderators was positioned on either side of the laminar target to detect the π^+ following Σ^- production in hydrogen. The delayed positron from the $\pi^+ \to \mu^+ \to e^+$ decay chain indicated the production of a π^+. Details regarding these spectrometers are described by Hertzog [29].

C. X-ray spectroscopy system

Solid-state x-ray detectors can have absolute efficiencies of 20% or more and are capable of resolving doublets having separations of the same order as the Σ^- W fine-structure splitting (approximately 1 keV in the $10l$ level). Reverse electrode coaxial intrinsic Ge x-ray detectors were used because of their lower susceptibility to neutron-induced radiation damage and subsequent resolution degradation [30].

Signal processing for the solid-state x-ray detectors was divided into three functional parts: charge-sensitive preamplifier, shaping amplifier, and analog-to-digital conversion (ADC). The preamplifier and amplifier were made for the experiment by the Lawrence Berkeley Laboratory detector group. The ADC used was a Lecroy 3511.

Low intensity (≈ 1 μCi) sources of γ rays of well-known energies [31, 32] provided calibration lines in the region of interest (see Table III) without interfering with the lines that were studied.

IV. DATA ANALYSIS

A. Off-line analysis

For photon energies between 77 and 750 keV, tagged events [KSTOP $\times$ (γ events followed by a delayed e^+ signal)] were histogrammed separately into spectra tag A, tag B, and tag C, depending on which detector recorded the x ray. The x-ray energies of those KSTOP $\times$ (γ events not followed by a delayed e^+ signal) (i.e., untagged) were histogrammed in spectra denoted raw A, raw B, and raw C. The improvement of the signal-to-noise ratio of the Σ^- x-ray lines due to tagging can be seen in Fig. 2, where we show the data near the $\Sigma^- 10l \to 9k$ transition at 505 keV in Pb (a) without tagging (untagged) and (b) with tagging (tagged). The intensity of kaonic transitions and background lines such as the annihilation peak at 511 keV is reduced by a factor of 80, while the intensity of Σ^- atomic transitions is cut by only a factor of 9. The photon energies recorded during beam-on events (events triggered by beam pions) were used to accumulate spectra from calibration sources in limited energy regions.

TABLE III. Absolute calibration energies.

Source	Energy (keV)	Used with target(s)
^{57}Co	122.063 $\pm$ 0.003[a]	Pb, W
	136.476 $\pm$ 0.003	
^{133}Ba	276.397 $\pm$ 0.012[a]	Pb
	302.839 $\pm$ 0.008	
	356.005 $\pm$ 0.017	
	383.851 $\pm$ 0.020	
^{192}Ir	205.79549$\pm$ 0.00007[b]	W
	295.95825$\pm$ 0.00001	
	308.45689$\pm$ 0.00001	
	316.50789$\pm$ 0.00001	
	468.07147$\pm$ 0.00027	
^{137}Cs	661.661 $\pm$ 0.003[b]	Pb, W
^{208}Pb $K^- 10k \to 8j$	499.276 $\pm$ 0.018[c]	Pb
^{184}W $K^- 10k \to 8j$	406.204 $\pm$ 0.012[c]	W

[a]Reference [31].
[b]Weighted mean of values from Ref. [32].
[c]Calculated value. See Table IV.

B. Detector response functions

Monoenergetic γ rays and x rays were used to determine the effective response function of the solid-state detectors. Spectra were fitted by the method of least-squares to a functional form consisting of a modified Gaussian on a quadratic background. It was found that it was necessary to add exponential tails to the Gaussians as discussed by Routti and Prussin [33] in order to get acceptable fits to the high statistics background lines such as the 511 keV annihilation peak shown in Fig. 2. Empirically it was observed that the tails on both the upper and lower sides of the Gaussians were of equal strength and shape as the line shapes were remarkably symmetric. An alternative method has been proposed by Roberts *et al.* [34].

The full width at half maximum (FWHM) of the Gaussian was found to be typically 1200 eV for the transi-
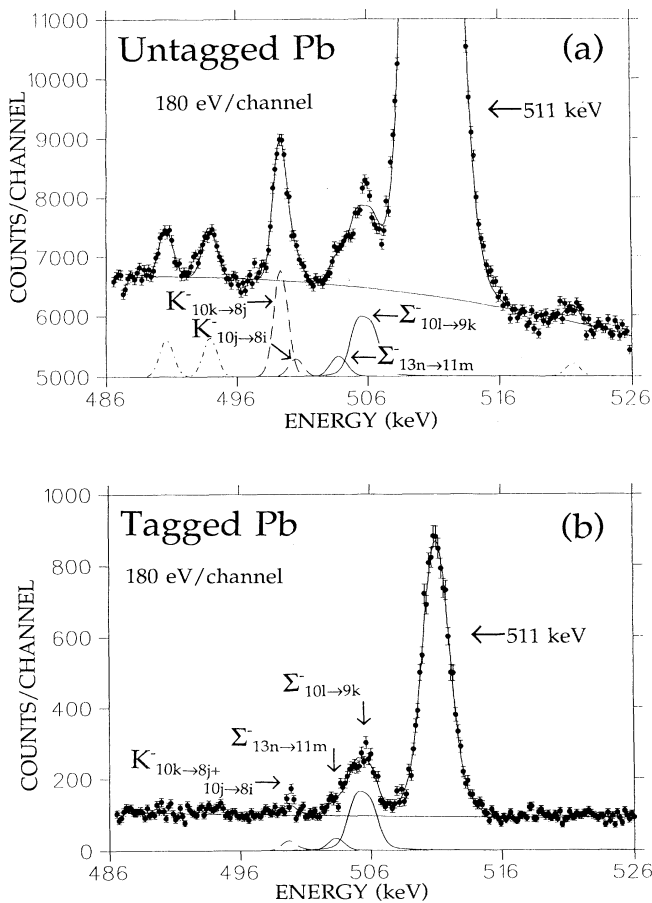
FIG. 2. A portion of the energy spectrum in the region of the Pb $\Sigma^- 10l \rightarrow 9k$ transitions from (a) untagged and (b) tagged histograms showing the dramatic effect of tagging on the Σ^- x-ray signal-to-noise ratio. The solid curves show the best fits to the data for a quadratic background. Beneath the data are the separated contributions from the Σ^- transitions (solid lines), the kaonic transitions (dashed lines), and the background nuclear gamma rays (dash-dotted lines). The 511-keV annihilation peak has been truncated to allow a better scale for the data of interest.

tions of interest. We took advantage of the $K^- 10k \rightarrow 8j$ transitions which occur about 6 keV below the $\Sigma^- 10l \rightarrow 9k$ transitions of interest in Pb and W to furnish both absolute calibration and detector response information. The calculated K^- binding energies are given in Table IV for the average kaon mass given by the Particle Data Group [8].

Barely resolvable on the high energy side of the kaonic $10k \rightarrow 8j$ transitions are the weak (13%) $10j \rightarrow 8i$ transitions, which were measured to lie 1.24(15) keV higher than the $10k \rightarrow 8j$ transitions in Pb. The calculated difference in energy is 0.896(13) keV taking into account the 36 eV kaonic strong interaction shift in the $8i$ level predicted with the optical potential for the kaon-nuclear strong interaction given by Batty [17].

The 6 eV per nucleon isotope shift in the kaonic $10l \rightarrow 9k$ transitions in natural Pb has been corrected for the isotopic composition given in Table II. In W the correction is about 5 eV per nucleon. For the kaon-nucleon strong interaction, the optical potential predicts the broadening of the Pb kaonic line to be less than 2 eV and the shift less than 1 eV. Hence, we may apply exactly the same criteria of theoretical uncertainty that we used for our calculated Σ^--transition energies (without strong interaction effects). For the Pb $K^- 10k \rightarrow 8j$ transition the uncertainty is less than 12 eV. The energies of these transitions in W and Pb are listed with the other calibration sources in Table III.

V. RESULTS

A. Widths deduced from x-ray intensities in Σ^- atoms

The procedure for deducing the strong interaction width of the upper level of a transition in terms of the yield of the electromagnetic transition from that level has been discussed in the article by Backenstoss *et al.* [25]. This procedure requires the use of an atomic cascade calculation with and without strong interaction effects to determine the relationship between the yield of the transition and the width of the upper level.

We used a computer code based on that developed by Leon and Seki [35]. We began the cascade at n = 25, assuming that the initial distribution of angular momenta l could be described by a statistical distribution modified by an exponential weighting factor, i.e., $(2l + 1)e^{\alpha l}$. We fit the relative intensities of the transitions (normalized to the $12n \rightarrow 11m$ transition) listed in Table V for the distribution parameter α and the width of the upper level.

For the Σ^- Pb atom a best fit was obtained for $\alpha = 0.253(60)$ and $\Gamma(10l) = 17(3)$ eV. The fourth column of Table V shows the yields calculated with the strong interaction described by the best-fit two-parameter optical potential shown in Table VIII; the third column shows the yields as calculated without strong interactions. The transitions which are directly affected by the strong interaction via absorption in the upper level are so indicated. However, almost all transitions show an indirect effect of absorption in other levels, which affects the intensity of

TABLE IV. K^- binding energies (keV).

Z	A	State	KG[a] solution	Electron screening	Higher order vac. pol.	Nuclear polarization	Dynamic $E2$ shift	Strong interaction shift[b]	Total
82	208	$10k$	885.044	0.146	−0.055	0.003	0.0	0.0	885.136
		$10j$	885.694	0.154	−0.047	0.006	0.0	0.0	885.807
		$8j$	1384.428	0.062	−0.088	0.010	0.0	0.0	1384.412
		$8i$	1386.003	0.075	−0.085	0.022	0.0	−0.036	1385.979
74	184	$10k$	720.178	0.104	−0.032	0.002	0.001	0.0	720.252
		$10j$	720.629	0.110	−0.027	0.003	0.004	0.0	720.719
		$8j$	1126.447	0.043	−0.052	0.005	0.013	0.0	1126.456
		$8i$	1127.530	0.052	−0.050	0.012	0.029	−0.006	1127.567

[a]The solution of the Klein-Gordon equation including finite-size Coulomb correction and first-order vacuum polarization using the mass of the kaon from Ref. [8].

[b]The strong interaction shift was calculated using the optical potential parameters of Batty [17].

transitions feeding lower levels.

As will be described, the best-fit optical potential based on all existing data predicts a width for the $10l$ level in the Σ^- Pb atom that is two standard deviations smaller than the experimental value based on the yield of the $\Sigma^- 10l \to 9k$ transition. This result is reflected in a predicted yield for the $10l \to 9k$ transition in Pb, which is two standard deviations too large.

For the W data a least-squares fit of the Σ^- atomic x-ray intensities yielded a value of $-0.090(29)$ for the distribution parameter α and a width of $\Gamma(10l) = 2(2)$ eV. The intensities were predicted (with and without strong interaction effects) with a cascade calculation beginning at $n=25$ and the best-fit two-parameter optical potential. These intensities agree reasonably well with our earlier data [1], except for the sum yield of the $10l \to 9k$ and $13n \to 11m$ transitions. The detailed analysis of the present untagged data, which have 50% better statistics,

allowed us to identify adjacent background lines, which had artificially reduced the apparent yields of these Σ^- hyperon atomic transitions.

B. Directly measured widths and shifts

The functional form of the detector response function must be modified to describe transitions which have been broadened by the strong interaction. The intensity of emitted radiation for such transitions is generally assumed to follow a Lorentzian distribution.

Strictly speaking, the initial as well as the final state of the transition has a characteristic Lorentzian width. In practice, the width of the former is so much smaller that it may either be included as a slight final correction to the width value or ignored. The complete detector response function which should be fitted to these transitions is thus

TABLE V. Measured and calculated Σ^- atom x-ray yields Y relative to the $12 \to 11$ transitions. Strong interaction (S.I.) effects were calculated with $\bar{a} = 0.280 + i0.133$ fm. The cascade began at $n=25$, with $\alpha(W) = -0.09$ and $\alpha(Pb) = 0.25$ (see text).

Σ^--W transition	Y (measured)	Y (calculated) No S.I.	Y (calculated) S.I. included
$14 \to 13$	0.95 ± 0.16	0.768	0.809
$13 \to 12$	1.04 ± 0.12	0.879	0.913
$12 \to 11$	1.00	1.000	1.000
$11 \to 10$[a]	1.07 ± 0.08	1.133	1.040
$10 \to 9$[a]	0.87 ± 0.06	1.154	0.896
$14 \to 12$	0.20 ± 0.02	0.222	0.211
$13 \to 11$	0.22 ± 0.02	0.236	0.204
$12 \to 10$[a]	0.18 ± 0.04	0.247	0.175
Σ^--Pb transition	Y (measured)	Y (calculated) No S.I.	Y (calculated) S.I. included
$15 \to 14$	0.82 ± 0.23	0.808	0.826
$14 \to 13$	0.92 ± 0.17	0.882	0.900
$13 \to 12$	0.95 ± 0.08	0.946	0.961
$12 \to 11$	1.00	1.000	1.000
$11 \to 10$[a]	1.01 ± 0.03	1.047	0.974
$10 \to 9$[a]	0.50 ± 0.04	1.087	0.598
$15 \to 13$	0.091 ± 0.018	0.089	0.090
$14 \to 12$	0.079 ± 0.017	0.085	0.084
$13 \to 11$	0.078 ± 0.016	0.077	0.073

[a]Directly affected by strong interactions.

a convolution of a Lorentzian with the detector response function.

Unfortunately, it was not possible to find an effective algorithm to calculate the terms involved in this response function short of a direct numerical evaluation of the convolution integral. This numerical evaluation provided adequate values for the response function, but required large amounts of computation time and ultimately did not provide the derivatives needed for the application of a least-squares fitting algorithm.

If the detector response function were Gaussian, the line shape would be the real part of a complementary (complex) error function. A convenient algorithm based on the method of continued fractions exists for the evaluation of the Voight (i.e., Gaussian-Lorentzian) integral [36]. This algorithm was incorporated into the least-squares fitting software as a useful, although clearly incomplete, approximation of the detector response function. We used the same Gaussian detector response function for both the absolute calibration line ($K^-10k \rightarrow 8j$ transition) and the $\Sigma^-10l \rightarrow 9k$ transition of interest in order to minimize the systematic uncertainty associated with not having an ideal detector response function. Fortunately in this experiment the actual detector response function was very symmetric and the non-Gaussian portion was not large.

The $\Sigma^-10l \rightarrow 9k$ transitions are actually three transitions whose energies differ by the fine-structure splittings in the initial and final states. In ^{208}Pb the $10l$ level has a fine-structure splitting of 1.5 keV. In principle the strong interaction effects need not be identical in both fine-structure components. However, our present experimental system is not sensitive enough to distinguish such differences. In our fits we used the calculated fine-structure splittings and relative intensities of the triplet components given by Bethe and Salpeter [37] assuming the fine-structure components are populated statistically. This allowed us to fit for an effective or averaged shift and width associated with each triplet.

A few keV below the Σ^- transitions of interest were weak ($\approx 15\%$ relative to the $10l \rightarrow 9k$ transitions) triplets corresponding to $13n \rightarrow 11m$ and $13m \rightarrow 11l$ transitions, which are completely unaffected by the strong interaction. (The latter triplet was assumed to have 30% of the intensity of the former triplet as predicted by our cascade calculations.) Fortunately in Pb these lines are partially resolved and can be fitted independently of the $10l \rightarrow 9k$ transitions. These lines can be seen in Fig. 2 as a shoulder on the left side of the $10l \rightarrow 9k$ lines. In ^{208}Pb we found the energy of the high energy component of the $13n \rightarrow 11m$ triplet to be 503.859(88) keV in fair agreement with the theoretical value 503.731(25) keV, which can be deduced from the binding energies given in Table I. In W we were able to resolve this triplet in the tagged spectrum only. An additional background line at 408.954(48) keV masked these triplets in the untagged W spectrum.

The fitted Pb data are shown in Fig. 2. We fitted a 40-keV wide region containing eight groups of peaks near the annihilation peak at 511 keV. As mentioned above, these included the kaonic $10k \rightarrow 8j$ and $10j \rightarrow 8i$ tran-

sitions, the former line being used to determine the absolute calibration. Besides the $\Sigma^-10l \rightarrow 9k$ transitions and the weak $\Sigma^-13n \rightarrow 11m$ transitions (along with its weak companion peaks corresponding to the $13m \rightarrow 11l$ transitions), we also fitted background lines occurring at 490, 493, 511, and 521 keV. It is likely that at least part of the somewhat broadened structure at 493 keV is due to a nuclear transition in ^{74}Ge resulting from inelastic scattering of neutrons in the detectors. There seems to be an additional structure at 507 keV in the untagged spectrum, which we did not include in the fit. However, it is much reduced in the tagged spectrum. The resolution of the system in the energy range of interest was determined from all unbroadened lines (i.e., excluding the broadened annihilation peak and the Pb $\Sigma^-10l \rightarrow 9k$ transitions) and was found to be 1260 eV. We determined the centroid and broadening of the Pb $\Sigma^-10l \rightarrow 9k$ transitions from the fit to the tagged spectrum also shown in Fig. 2. In this spectrum the 511 peak and remnants of the kaonic $10k \rightarrow 8j$ are the only background (non-
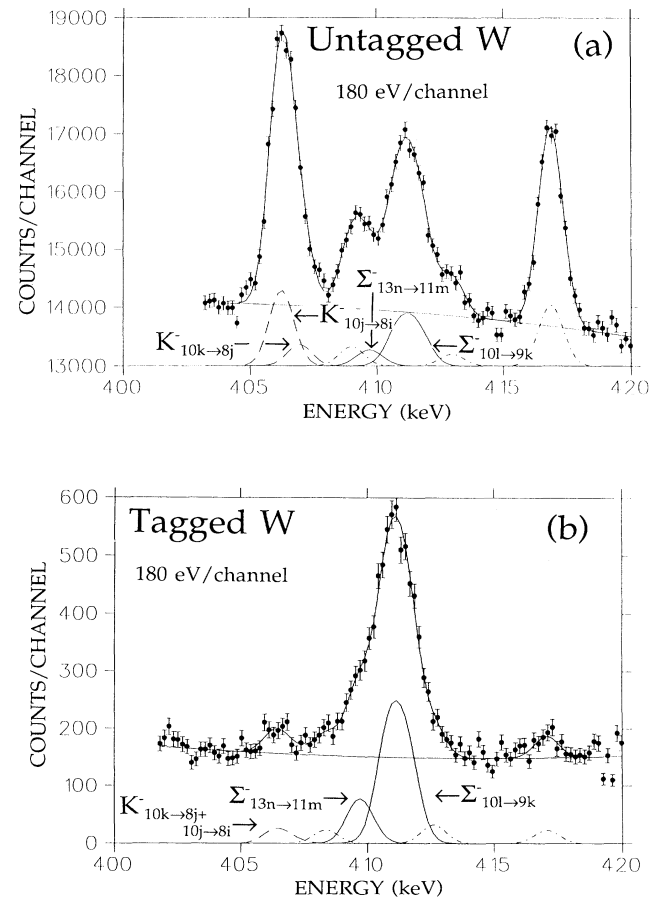
FIG. 3. A portion of the energy spectrum in the region of the W $\Sigma^-10l \rightarrow 9k$ transitions from (a) untagged and (b) tagged histograms. The solid curves show the best fits to the data for a quadratic background. Beneath the data are the separated contributions from the Σ^- transitions (solid lines), the kaonic transitions (dashed lines), and the background nuclear gamma rays (dash-dotted lines).

Σ hyperon atomic transitions) lines which remain. The measured strong interaction shifts and widths for the Pb $\Sigma^-10l \to 9k$ transitions are listed in Table VI.

The fitted W spectra appear in Fig. 3. In the untagged spectrum, besides the $K^-10k \to 8j$ and $10j \to 8i$ and $\Sigma^-13n \to 11m$ and $13m \to 11l$ transitions mentioned above, there are contributions from peaks at 408.954(49), 412.928(74), and 416.823(33) keV. The last peak undoubtedly corresponds to the 416.852(3) keV [38] nuclear γ ray from ^{26}Al as a result of (x,xn) interactions (where x is any particle producing a knockout neutron) in the aluminum housing of the detector. The sources of the other contaminant lines are unidentified and would pose an unpleasant problem for determining the energy of the W $\Sigma^-10l \to 9k$ transitions at 411.115(53) keV were it not for the fact that they essentially vanish in the tagged spectrum. As in the case of Pb, we were able to fit for the two kaonic transitions. We found the W kaonic $10j \to 8i$ transition energy to be 406.896(100) keV, which is in excellent agreement with the expected energy of 406.849(9) keV, determined by adding the expected strong interaction shift of 6.1 eV in the $8i$ level (given by the Batty [17] kaonic optical potential) to the binding energies given in Table IV. The detector resolution at this energy determined from the kaonic transitions and the ^{26}Al nuclear γ ray was 1130 eV. The measured transition energy, strong interaction shift, and the broadening of the $\Sigma^-10l \to 9k$ transitions in W, corrected for isotopic composition and expressed relative to ^{184}W, are given in Table VI.

C. Effective scattering lengths

The effective optical potential as described in Eq. (1) was then fitted to existing data in even-even nuclei and to our measured shifts and widths in Σ^- hyperonic Pb and W. We tried both a two-parameter fit corresponding to an isospin independent optical potential and a four-parameter fit, which effectively permits different two-parameter optical potentials for protons and for neutrons. The data used in the fit are shown in Table VII. To make the isospin-dependent optical potential more realistic we allowed the neutron and proton radii to be different. For the lighter elements we used the theoretical predicted values for Δ_{n-p} (the difference of the root mean square radii of the proton and neutron distributions) by Auger [22], who used a Hartree-Fock procedure with BCS pairing. For ^{208}Pb we used the Hartree-Fock-Bogolyubov calculations of Decharge and Gogny [23]. For ^{138}Ba and ^{184}W we interpolated between the values given in Ref. [23] for Sn and Pb. These values are also given in Table VII. The best-fit nuclear optical potential parameters are given in Table VIII. For comparison, we include the values of Batty [18], who fitted all the data extant before this experiment and assumed that $\Delta_{n-p} = 0.0$ fm.

The fitted strong interaction effects from our four-parameter fit are shown in the sixth column of Table VII. The ratio of the difference of the experimental and fitted values to the total error (experimental and theoretical) is shown in the last column in order to indicate which data fit well and which do not. This ratio is essentially the square root of the contribution to the χ^2. It is important to point out that the only nuclei with precise strong interaction measurements which are expected to exhibit sizeable isospin effects are those for which $Z \neq A - Z$. The only two nuclei in this list with these characteristics are Pb and W.

The major improvement in the quality of the four-parameter fit over the two-parameter one results from the better description of the shift and upper level width in the Si $5g \to 4f$ transition and the lower level width in the Pb $10l \to 9k$ transition. At the present time these two nuclei seem to be more sensitive to isovector effects because of the higher precision of the measurements. In many of the other measurements the experimental error is comparable to the strong interaction effect measured.

VI. DISCUSSION AND CONCLUSIONS

A reasonably good representation of the strong interaction effects due to the hadronic interaction between the Σ^- hyperon and nuclei can be found by using a two-parameter isospin-independent optical potential, even if one includes high-Z nuclei, where one might expect isospin effects to be significant. If one tries to include two

TABLE VI. Energies of the $10l$ to $9k$ transitions in Σ^- Pb and W.

Z	A	Predicted transition energy[a] (keV)	Transition energy $10l \to 9k$ (keV)	Relative yield[c] $10l \to 9k$	Shift $9k$ (eV)	Width $9k$ (eV)	Deduced width $10l$ (eV)
					Strong interaction		
				Measured observables[b]			
82	208	504.899(28)[d]	505.321(48)	0.46(5)	422(56)	428(158)	17(3)
74	184	410.901(29)[d]	411.115(53)	0.71(6)	214(60)	18(149)	2(2)

[a]Electromagnetic effects only.
[b]Corrected for the effects due to other isotopes in the targets of natural isotopic composition and to the presence of $13n \to 11m$ and $13m \to 11l$ transitions.
[c]The ratio of the measured to calculated (assuming no strong interactions) intensity of the $10l \to 9k$ transitions.
[d]Error in predicted transition energy includes the uncertainty in the mass of the Σ^- hyperon, 20% of the nuclear polarization correction, and 5% of the dynamic $E2$ shift.

TABLE VII. Σ^- hyperon atomic data fitted to optical potential.

Z	A	$\Delta_{n-p}{}^c$ (fm)	Observable	Experimental energy[a] (keV)	Fitted energy[b] (keV)	Difference/error
6	12	-0.016	$\Gamma(3d)$	$0.031(12)^d$	0.036	0.45
8	16	-0.024	$4f \to 3d$	$92.760(23)^e$	92.724	-0.16
			$\Gamma(4f)$	$0.0010(17)^e$	0.0003	-0.40
12	24.3	-0.033	$5g \to 4f$	$98.77(4)^e$	98.786	0.40
			$\Gamma(4f)$	$<0.070^e$	0.043	0.24
			$\Gamma(5g)$	$0.00011(9)^e$	0.00005	-0.67
14	28	-0.034	$5g \to 4f$	$135.56(4)^e$	135.524	-0.90
			$\Gamma(4f)$	$0.22(11)^e$	0.228	-0.07
			$\Gamma(5g)$	$0.0004(1)^e$	0.00031	-0.90
16	32	-0.041	$5g \to 4f$	$178.28(22)^e$	178.376	0.44
			$\Gamma(4f)$	$0.87(70)^e$	1.133	0.38
			$\Gamma(5g)$	$0.0015(8)^e$	0.0019	0.44
20	40	-0.040	$\Gamma(6h)$	$0.00041(22)^d$	0.00009	-1.39
22	48	0.081	$\Gamma(6h)$	$0.00065(42)^d$	0.00040	-0.60
56	138	0.14	$\Gamma(9k)$	$0.0029(35)^d$	0.0004	-0.72
74	184	0.13	$10l \to 9k$	$411.115(53)^f$	410.968	-2.23
			$\Gamma(9k)$	$0.018(149)^f$	0.102	0.56
			$\Gamma(10l)$	$0.002(2)^f$	0.001	-0.50
82	208	0.13	$10l \to 9k$	$505.321(48)^f$	505.299	-0.44
			$\Gamma(9k)$	$0.428(158)^f$	0.736	1.95
			$\Gamma(10l)$	$0.017(3)^f$	0.011	-2.00

[a] The uncertainty quoted here includes the experimental error as well as the theoretical uncertainty in calculating the transition energies.

[b] Using the results of the four-parameter fit given in Table VIII.

[c] Theoretical values for the difference of the root mean square radii of the proton and neutron distributions taken from Refs. [22, 23].

[d] Data taken from Ref. [25].

[e] Data taken from Ref. [26].

[f] Data from this experiment.

extra parameters to give an isospin dependence to the optical potential, the quality of the fit improves somewhat more than would be expected merely from the addition of two additional parameters. Although the best-fit values of the two added isovector parameters are nonzero, the errors of the fitted parameters do not strongly exclude zero values.

The data from the Pb nucleus contribute most to the χ^2. But even in this case, the largest difference between experimental and predicted values is barely two standard deviations. Indeed only four of the twenty-one observables differ from the values predicted by the four-parameter optical potential by more than one standard deviation. It is clear that if one is interested in studying

isospin effects with Σ^- atoms, one must use separated isotopes.

TABLE VIII. Fitted Σ^--nuclear optical potential parameters.

a_0	a_1	$\chi^2/N_{DF}{}^a$
$0.361(44) + i\,0.157(27)$	$-0.34(17) - i\,0.17(11)$	19.55/17
$0.280(20) + i\,0.133(17)$	$0.0 + i\,0.0$	25.03/19
$0.363(48) + i\,0.202(25)^b$	$0.0 + i\,0.0$	12.2/15

[a] N_{DF} is the number of degrees of freedom.

[b] Fit of earlier data by Batty [18], assuming $\Delta_{n-p} = 0.0$ fm.

to thank Dr. D. Lowenstein and the Brookhaven Alternating Gradient Synchrotron staff for their support, and R. Meier for the design and construction of the laminar liquid-hydrogen target. We appreciate the efforts of C. A. Lasota for assistance with the data analysis and the cascade programs. We wish to thank Dr. L. Rosen of the Los Alamos Meson Physics Facility for the use of the LAMPF test beam and Dr. N. J. Colella, Dr. K. L. Giovanetti, and Dr. R. D. Hart for their help on the earlier phases of the experiment. One of us (R.J.P.) appreciates the hospitality of Professor S. Koonin and his colleagues at the Kellogg Radiation Laboratory of the California Institute of Technology, where a part of the analysis was completed.

[1] D. W. Hertzog, M. Eckhause, P. P. Guss, D. Joyce, J. R. Kane, W. C. Phillips, W. F. Vulcan, R. E. Welsh, R. J. Whyley, R. G. Winter, E. Austin, J. P. Miller, F. O'Brien, B. L. Roberts, G. W. Dodson, R. J. Powers, R. B. Sutton, and A. R. Kunselman, Phys. Rev. D **37**, 1142 (1988).

[2] K. P. Gall, E. Austin, J. P. Miller, F. O'Brien, B. L. Roberts, D. R. Tieger, G. W. Dodson, M. Eckhause, J. Ginkel, P. P. Guss, D. W. Hertzog, D. Joyce, J. R. Kane, C. Kenney, J. Kraiman, W. C. Phillips, W. F. Vulcan, R. E. Welsh, R. J. Whyley, R. G. Winter, R. J. Powers, R. B. Sutton, and A. R. Kunselman, Phys. Rev. Lett. **60**, 186 (1988).

[3] E. Borie and G. A. Rinker, Rev. Mod. Phys. **54**, 67 (1982).

[4] E. Borie, Phys. Rev. A **28**, 555 (1983).

[5] E. Borie and B. Jödicke, Comput. Phys. **2**(6), 60 (1988).

[6] R. J. Powers, F. Boehm, P. Vogel, A. Zehnder, T. King, A. R. Kunselman, P. Roberson, P. Martin, G. H. Miller, R. E. Welsh, and D. A. Jenkins, Nucl. Phys. **A262**, 493 (1976).

[7] J. Schwinger, Phys. Rev. **75**, 651 (1949).

[8] Particle Data Group, Phys. Rev. D **45**, S1 (1992).

[9] J. Blomqvist, Nucl. Phys. **B48**, 95 (1972).

[10] P. Vogel, At. Data Nucl. Data Tables **14**, 599 (1974).

[11] R. C. Barrett, S. J. Brodsky, G. W. Erickson, and M. H. Goldhaber, Phys. Rev. **166**, 1589 (1968).

[12] T. E. O. Ericson and J. Hüfner, Nucl. Phys. **B47**, 205 (1972).

[13] B. Fricke, Phys. Rev. Lett. **30**, 119 (1973).

[14] J. L. Friar and J. W. Negele, Phys. Lett. **46B**, 5 (1973).

[15] D. Hitlin, S. Bernow, S. Devons, I. Duerdoth, J. W. Kast, E. R. Macagno, J. Rainwater, and C. S. Wu, Phys. Rev. C **1**, 1184 (1970).

[16] R. Engfer, H. Schneuwly, J. L. Vuilleumier, H. K. Walter, and A. Zehnder, At. Data Nucl. Data Tables **14**, 509 (1974).

[17] C. J. Batty, Nucl. Phys. **A372**, 418 (1981).

[18] C. J. Batty, Nucl. Phys. **A372**, 433 (1981).

[19] T. Yamada, Y. Yamamoto, J. Zofka, and M. Sotona, in abstracts submitted to the International Symposium on Hypernuclear and Strange Particle Physics, Shimoda, Japan, 1991 (unpublished).

[20] G. Höhler, E. Pietarinen, I. Sabba-Stefanescu, F. Borkowski, G. G. Simon, V. H. Walther, and R. D. Wendling, Nucl. Phys. **B114**, 505 (1976).

[21] R. Kunselman, R. J. Powers, M. V. Hoehn, and E. B. Shera, Nucl. Phys. **A405**, 627 (1983).

[22] J. P. Auger, thesis, Université Paris-Sud, Centre d'Orsay (1977), unpublished.

[23] J. Decharge and D. Gogny, Phys. Rev. C **21**, 1568 (1980).

[24] R. J. Powers, K.-C. Wang, M. V. Hoehn, E. B. Shera, H. D. Wohlfahrt, and A. R. Kunselman, Nucl. Phys. **A336**, 475 (1980).

[25] G. Backenstoss, T. Bunaciu, J. Egger, H. Koch, A. Schwitter, and L. Tauscher, Z. Phys. A **273**, 137 (1975).

[26] C. J. Batty, S. F. Biagi, M. Blecher, S. D. Hoath, R. A. J. Riddle, B. L. Roberts, J. D. Davies, G. J. Pyle, G. T. A. Squier, and D. M. Asbury, Phys. Lett. **74B**, 27 (1978).

[27] D. Zieminska, Phys. Lett. **37B**, 403 (1971).

[28] D. J. Miller, R. J. Nowak, and T. Tymieniecka, in *Low and Intermediate Energy Kaon-Nucleon Physics*, Rome, 1980, edited by F. Ferrair and G. Violini (Reidel, Dordrecht, 1981), p. 251.

[29] D. W. Hertzog, Ph.D. thesis, College of William and Mary, 1983 (unpublished).

[30] R. H. Pehl, N. W. Madden, J. H. Elliott, T. W. Raudorf, R. C. Trammel, and L. S. Darken, Jr., IEEE Nucl. Sci. Symp., Washington, D.C. (1978).

[31] K. Debertin, PTB Report PTB-Ra-12 (1980).

[32] *Table of Isotopes*, 7th Ed., edited by C. M. Lederer and V. S. Shirley (Wiley, New York, 1978).

[33] J. T. Routti and S. G. Prussin, Nucl. Instrum. Methods **72**, 125 (1969).

[34] B. L. Roberts, R. A. J. Riddle, and G. T. A. Squier, Nucl. Instrum. Methods **130**, 559 (1975).

[35] M. Leon and R. Seki, Phys. Rev. Lett. **32**, 132 (1974).

[36] C. J. Batty, S. D. Hoath, and B. L. Roberts, Nucl. Instrum. Methods **137**, 179 (1976).

[37] H. A. Bethe and E. E. Salpeter, *Quantum Mechanics of One- and Two-Electron Atoms* (Springer-Verlag, Berlin, 1957), p. 274.

[38] P. M. Endt, Nucl. Phys. **A521**, 1 (1990).